Exp. Theo. NANOTECHNOLOGY 10 (2026) 995-1011 https://doi.org/10.56053/10.S.995

Correlation between manganese variation, microstructure, shape memory behavior, ion release and nanotechnology-relevant features of Cu–Al–Mn alloys

S M N Ahmed[1], *A M Mustafa*[1], *F F Sayyid*[1], *Makaram H. Abdulkareem*[1], *Alaa Fadel Aidan*[2], *Mohammed RASHEED*[1,*]

[1]College of Production Engineering & Metallurgy, University of Technology- Iraq, Baghdad 10066, Iraq
[2]Training and Workshop Center- University of Technology- Iraq, Baghdad 10066, Iraq
[*]) Email: rasheed.mohammed40@yahoo.com

Received 4/2/2026, *Received in revised form* 24/3/2026, *Accepted* 18/4/2026, *Published* 15/5/2026

Cu–Al–Mn shape memory alloys (SMAs) are synthesized via powder metallurgy with Mn contents ranging from 1 to 9 wt.% while maintaining constant Al levels. The influence of Mn on microstructure, phase transformation, hardness, and chemical stability is systematically evaluated. Optical and SEM analyses showed a clear refinement of martensitic plates as Mn increased, progressing from coarse, well-defined variants in low-Mn alloys to fine, densely packed lamellae with partial β-phase retention in high-Mn compositions. XRD confirmed the presence of the martensitic Cu–Al–Mn phase with minor $AlCu_3$ peaks, alongside lattice contraction indicated by peak shifts. DSC revealed a substantial decrease in Ms, Mf, As, and Af with higher Mn, demonstrating β-phase stabilization. Hardness increased consistently due to solid-solution strengthening and martensitic refinement. Ion-release measurements showed enhanced chemical stability in high-Mn alloys, with CuAlMn5 exhibiting the lowest dissolution level. Overall, Mn effectively tailors structural and functional performance in Cu–Al–Mn SMAs. From a nanotechnology perspective, the progressive refinement of martensitic structures observed with increasing Mn content introduces nanoscale and sub-microscale features that are highly relevant for advanced functional materials. The formation of fine lamellar martensite, increased variant subdivision, and stabilized β-phase structures directly influence surface reactivity, ion release behavior, and mechanical response at small length scales. Such nanoscale microstructural

control positions Cu–Al–Mn shape memory alloys as promising candidates for nanotechnology-driven applications, including micro-actuators, biomedical devices, and corrosion-resistant smart materials.

Keywords: Cu-Al-Mn alloy; Shape memory alloys; Hardness; Microstructure.

1. INTRODUCTION

Shape memory alloys (SMAs) comprise several types of functional metals that would retain their original shape when subjected to elevated temperatures or heat. SMAs can generally be grouped into two major categories based on its material makeup - copper based SMAs (such as Cu-Zn-Al, Cu-Al-Ni and Cu-Al-Mn alloys) and nickel titanium based SMAs (such as Ni-Ti, Ni-Ti-Cu and Ni-Ti-Nb alloys). Additionally, many different processes exist and can be used to produce SMAs ranging from induction melting techniques, vacuum melting methods, electron beam melting processes, powder metallurgy routes, rapid solidification methods and mechanical alloying methods that can be performed on either small laboratory scales or large-scale industrial operations. Martensitic phase transformations of copper aluminum nickel based SMAs have been studied and documented extensively, resulting in extensive amounts of evidence to demonstrate that a large amount of martensite is developed through the various metals used to manufacture the alloy. The β phase of copper aluminum nickel based SMAs that exist at ambient temperature exhibit multiple phases of order-disorder transformation i.e. long period stacking ordered martensites – (3R, 9R, 2H). There are three different types of martensite that can be developed from the thermal treatment and chemical composition of the steel; these are termed α1, β1 and γ1 [2, 3]. An increased amount of aluminum in the alloy will aid in the transformation from β to γ1; however, adding nickel provides greater stability to the β1-type of martensite [8,9].

Research is being conducted on Cu-Al-Mn alloys as a possible alternative to Cu-Al-Ni alloys as they have many advantages over Cu-Al-Ni including, lower cost, improved machinability, increased pseudoelasticity and thermal stability. In addition to the previously mentioned advantages Cu-Al-Mn alloys can also be engineered to have varying transformation temperatures based on the chemical composition of the alloy; therefore, allowing for many different engineered applications. Manganese plays a vital role in Cu-Al-Mn alloys because it contributes to stabilizing the β phase in addition to reducing the formation of β2 intermetallic. Manganese also assists in refining the microstructure of the alloy and has an effect on the martensitic transformation temperatures and mechanical properties of the alloy. The addition of manganese changes the e/a (electron to atom) ratio, which will ultimately affect phase stability and performance of the alloy. Cu-Al-Mn alloys are considered very well suited to the powder metallurgy process due to the increase in ductility of the alloy by the addition of Mn. The powder metallurgy process produces a finer microstructure and more uniform properties than the cast alloys [16,17].

There are many advantages to Cu-Al-Mn SMAs but there are still some impediments to developing these materials due to the conventional melting techniques. These techniques can produce micro-segregation effects, large grain size and secondary phase formation, which compromise overall mechanical reliability [18,19]. In addition, little has been published on systematic studies of Cu-Al-Mn alloy processed through powder metallurgy, but many studies have been done on cast metals [20,21]. Specifically, only minimal integrated research exists evaluating the impact of incremental additions of Mn on the microstructure, transformation temperature, hardness, functional performance or chemical reliability [22,23]. This aspect is of concern because ion release into an aqueous/physiological

environment will affect the long-term performance of the material and its potential biocompatibility; however, there has not been much research into the latter [24,25].

This research fills an important knowledge gap by determining how adding varying amounts of manganese to copper-aluminum-manganese shape memory alloys as made from powder metallurgy techniques will influence two properties of those alloys. A variety of complementary experimental techniques (light microscopy, scanning electron microscopy with energy dispersive spectroscopy, X-ray diffraction, differential scanning calorimetry, microhardness and shape recovery tests, and inductively coupled plasma optical emission spectrometry) are used to gain a comprehensive and unified understanding of the relationship between the amount of manganese in the alloy, the microstructure. metallurgical characteristics, and the resulting mechanical and corrosion characteristics. An empirical relationship (composition-structure-property) for Cu-Al-Mn shape memory alloys will also be established for use by future engineers and may be beneficial to both functional and biomedical applications that have been designed to optimise shape memory behaviour. This article describes the fabrication, characterization, and evaluation of copper-aluminum-manganese shape memory alloys manufactured using powder metallurgy and varying levels of manganese, and will provide direction for future design and use of these materials.

Nanotechnology has increasingly emphasized the importance of controlling material behavior at the nano- and sub-micrometer scales, where surface-to-volume ratio, interface density, and defect distribution strongly influence functional performance. In shape memory alloys, nanoscale refinement of martensitic variants and phase interfaces can significantly affect transformation characteristics, mechanical strength, and chemical stability. Cu–Al–Mn alloys, in particular, exhibit compositional tunability that enables the development of nanostructured martensitic morphologies through alloying and powder-metallurgy processing. Understanding how Mn content governs these nanoscale features is therefore essential for designing Cu–Al–Mn SMAs for emerging nanotechnology-enabled applications.

2. EXPERIMENTAL WORK

High-purity elemental powders of copper (Cu, ≥99.9%), aluminium (Al, ≥99.9%), and manganese (Mn, ≥99.9%) are used to prepare a series of Cu–Al–Mn alloys in which the Al content is fixed at 14 wt.% and the Mn content is varied from 1 to 9 wt.% at the expense of Cu. Five compositions are produced: CuAlMn1 (85Cu–14Al–1Mn), CuAlMn2 (83Cu–14Al–3Mn), CuAlMn3 (81Cu–14Al–5Mn), CuAlMn4 (79Cu–14Al–7Mn), and CuAlMn5 (77Cu–14Al–9Mn). The powders are weighed accurately, placed into a sealed milling vial, and homogenized using a planetary ball mill at 200 rpm for 4 h under an argon atmosphere to prevent oxidation. A ball-to-powder weight ratio of 5:1 is employed, and intermittent milling cycles are used to minimize overheating and excessive cold welding. The homogenized powders are then compacted into cylindrical pellets using a uniaxial hydraulic press with a 10 mm diameter steel die. Each sample is pressed under a 5-ton load (approximately 600–650 MPa) and held for 30–60 s before ejection to improve green density.

The green compacts are subjected to a calcination/sintering heat treatment to enhance interdiffusion and densification. Samples are placed in alumina boats and heated in a tube furnace under flowing argon at a rate of 10 °C/min to approximately 850 °C, held for 2 h, and then either furnace-cooled or water-quenched from the solutionizing temperature to stabilize the high-temperature β-phase characteristic of shape memory alloys. After sintering, the pellets are sectioned using a low-speed diamond saw, mounted in epoxy resin, and polished through standard metallographic procedures, including grinding with SiC papers (240–1200 grit) and polishing with 6 μm, 3 μm, and 1 μm diamond

suspensions. Etching with an appropriate Cu–Al alloy reagent is performed to reveal martensitic structures, grain boundaries, and secondary phases.

The powders are homogenized using a planetary ball mill (Retsch PM200, Germany) and subsequently compacted into pellets with a uniaxial hydraulic press (Carver Laboratory Press, USA). Heat treatment of the green compacts is performed in a controlled-atmosphere tube furnace (Nabertherm LHT Series, Germany), and the sintered samples are sectioned using a precision low-speed diamond saw (Buehler IsoMet 1000, USA). Microstructural observations are carried out using an optical microscope (Olympus BX51, Japan) and a scanning electron microscope equipped with EDS analysis (JEOL JSM-6510LV with Oxford X-Max EDS, Japan/UK). Phase identification is conducted using an X-ray diffractometer (PANalytical Empyrean, Netherlands), while martensitic transformation temperatures are measured using a differential scanning calorimeter (Netzsch DSC 204 F1 Phoenix, Germany). Mechanical properties are evaluated using a Vickers microhardness tester (Shimadzu HMV-2, Japan), and ion-release behavior is analyzed with an ICP-OES instrument (PerkinElmer Optima 8000, USA).

3. RESULTS AND DISCUSSION

3.1. EDS analysis

Table 1 Chemical composition of the Cu–Al–Mn (CAN) SMAs and martensitic transformation temperatures (Ms, Mf, As, Af) determined by DSC measurement. Alloys are prepared with fixed Al (14 wt%) and isothermally increased Mn concentrations from 1 to 9 wt%. That there is such a structure gradient variation makes it potentially possible to compare meaningfully, say, how an increase in Mn addition affects the transformation behavior of Cu–Al–Mn SMAs. As we see in Table 1 the samples all show clear forward (Ms, Mf) and reverse (As, Af) martensitic transformation temperatures, characteristic for shape memory alloys [11-14]. The amounts of transformation temperatures and their variation with Mn content are also presented in Table 1 and well-defined order evolution can be found with the increase in Mn contents [26,27]. The alloyed with the lowest Mn amount (CuAlMn1, 1 wt% Mn) exhibits the highest transformation temperatures i.e Ms and Af around 158.56 °C and 209.51 °C respectively. The Ms, Mf, As and Af temperatures all decrease with the addition of Mn to 3 and 5 wt% without corresponding removal owing to the obvious effect on lowering the thermal stability of the martensite phase [28,29]. This tendency remains in 9wt% Mn alloys, in which the Ms values decrease to 71.49 °C and 44.09 °C, respectively34), indicating that Mn can suppress martensitic precipitation [30]. Similarly, As and Af reverse transformation temperatures correspondingly decrease from 209.51 oC for 1 wt% Mn to 75.33 oC for of 9 wt% Mn [31-35]. This may be attributed to the fact that Mn influences the e/a ratio and destabilizes the reference β-parent phase. The high-temperature β-phase is stabilized with increasing Mn and lower temperature is required to induce the β→martensite transformation. It is found further that the Af value decreases gradually with an increase in Mn content, indicating that the energy for perfect reverse martensitic transformation (β→martensite) decreases as control concentration of Mn increases. This composition effect is widely acknowledged in Cu–Al–Mn alloys and thus expected, given the strong electronic and structural role of Mn in ternary systems.[36].

Table 1 demonstrates that manganese content is a key factor controlling the martensitic transformation range of Cu–Al–Mn alloys. The progressive reduction in Ms and Af temperatures with increasing Mn enables the tuning of these alloys for applications requiring lower transformation temperatures, improved functional stability, or compatibility with specific operating environments. Thus, the systematic interpretation of Table 1 highlights the importance of alloy design in tailoring the thermal and functional behavior of Cu–Al–Mn shape memory alloys.

Table 1 Composition of Cu-Al-Mn alloys and Ms and Af transformation temperatures.

Sample shape memory alloys	Cu wt.%	Cu At.%	Al wt.%	Al At. %	Mn wt.%	Mn At.%	K-ratio	Ms(oC)	Mf(oC)	As (oC)	Af (oC)
CuAlMn 1	85.4	66.9	13.8	31.6	0.8	1.5	0.78, 0.22, 0.015	158.56	170.82	180.17	209.51
CuAlMn 2	84.4	65.0	12.9	31.4	2.7	3.6	0.75,0.21,0.036	136.92	170.76	156.31	214.76
CuAlMn 3	82.7	63.4	13.1	31.2	4.2	5.4	0.73,0.20,0.054	132.87	158.98	138.6	164.67
CuAlMn 4	80.4	61.7	13.3	31.1	6.3	7.2	0.70,0.19,0.072	71.49	90.99	80.98	105.82
CuAlMn 5	78.8	59.9	12.6	30.9	8.6	9.2	0.67,0.18,0.092	44.09	72.64	55.31	75.33

3.2. SEM analysis

Across the series of Cu–Al–Mn alloys shown in Figure 1(a–e), a clear and progressive refinement of the martensitic microstructure is observed as the Mn content increases from 1 to 9 wt.%. The CuAlMn1 alloy exhibits coarse, widely spaced martensite plates indicative of a stable martensitic phase with high transformation temperatures, while CuAlMn2 and CuAlMn3 show increasingly finer and more densely packed variants, reflecting enhanced self-accommodation and the growing stabilizing effect of Mn on the β-phase. In the higher-Mn alloys, CuAlMn4 and CuAlMn5, the martensite becomes extremely fine, thin, and closely aligned, with regions of retained β-phase becoming more evident, consistent with the substantial lowering of Ms and Af temperatures. Together, the micrographs demonstrate that manganese plays a decisive role in suppressing martensite plate thickness, increasing variant subdivision, and reducing overall transformation temperature, resulting in the highly refined and partially transformed microstructure seen at the highest Mn content [36,37].

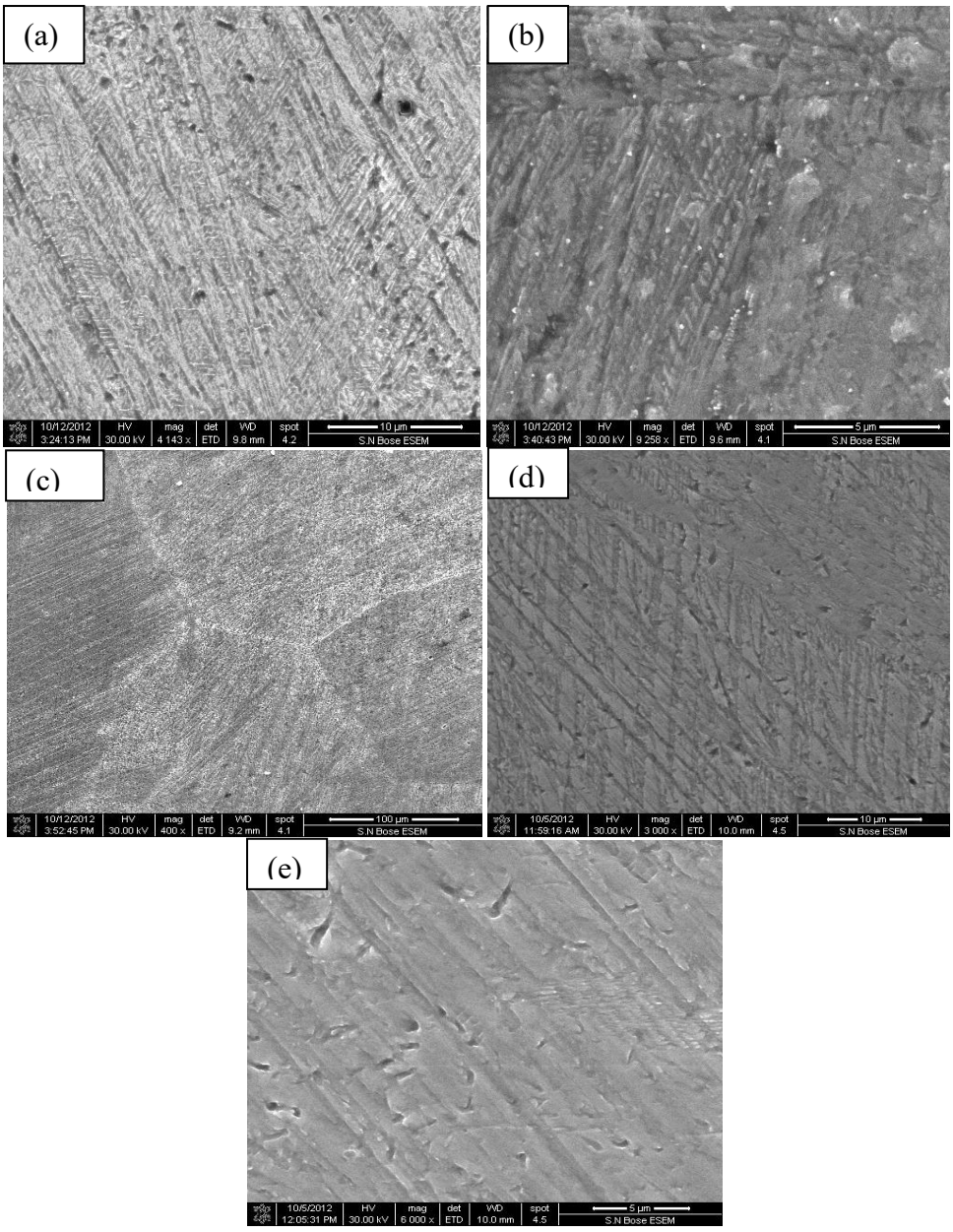

Figure 1 SEM micrographs of Cu–Al–Mn shape memory alloys with increasing Mn content: (a) CuAlMn1 (1 wt.% Mn), (b) CuAlMn2 (3 wt.% Mn), (c) CuAlMn3 (5 wt.% Mn), (d) CuAlMn4 (7 wt.% Mn), and (e) CuAlMn5 (9 wt.% Mn).

3.3. Optical microscope analysis

The optical microstructures of the Cu–Al–Mn alloys shown in Figure 2(a–e) reveal a clear and systematic evolution of martensitic morphology as the Mn content increases from 1 to 9 wt.%. In CuAlMn1 (Figure 1a), the microstructure is dominated by large, coarse, and widely spaced martensite plates, forming a typical basket-weave arrangement. These broad variants intersect at wide angles,

indicating a stable martensitic phase formed at relatively high transformation temperatures, consistent with the measured Ms and Af values for this composition. As the Mn content increases to 3 wt.% in CuAlMn2 (Figure 1b), the martensite plates become noticeably finer and more densely arranged, and multiple variant systems coexist within the same grain. This refinement reflects the increasing stabilizing effect of Mn on the high-temperature β-phase and the resulting reduction in the driving force for martensitic transformation. The trend becomes more pronounced in CuAlMn3 (Figure 1c), where the microstructure displays uniform, densely packed martensite colonies with significant internal variant subdivision. Although the image is at lower magnification, the refinement of the martensitic structure is evident, indicating that the alloy undergoes a complete transformation despite further decreases in Ms and Af temperatures [38-40]. In CuAlMn4 (Figure 1d), the martensitic lamellae become even thinner and more tightly aligned, forming highly oriented, fine plates distributed uniformly across the microstructure. The higher Mn content leads to pronounced refinement and increased crystallographic alignment, features characteristic of alloys with significantly lowered transformation temperatures and a more stable β-phase [38, 39]. Finally, CuAlMn5 (Figure 1e), containing 9 wt.% Mn, exhibits the finest and least distinctly resolved martensitic plates in the series. The microstructure appears smoother and more blended, with regions that likely correspond to retained β-phase or incomplete martensitic transformation. This behavior aligns with the lowest Ms and Af temperatures observed among all samples and reflects the strong suppression of martensitic formation at room temperature due to high Mn levels. Taken together, the optical micrographs demonstrate that increasing Mn content progressively refines the martensitic morphology, enhances variant subdivision, and promotes partial β-phase retention, fully supporting the thermal analysis and confirming the sensitive dependence of martensitic transformation on alloy composition in Cu–Al–Mn SMAs [40,41].

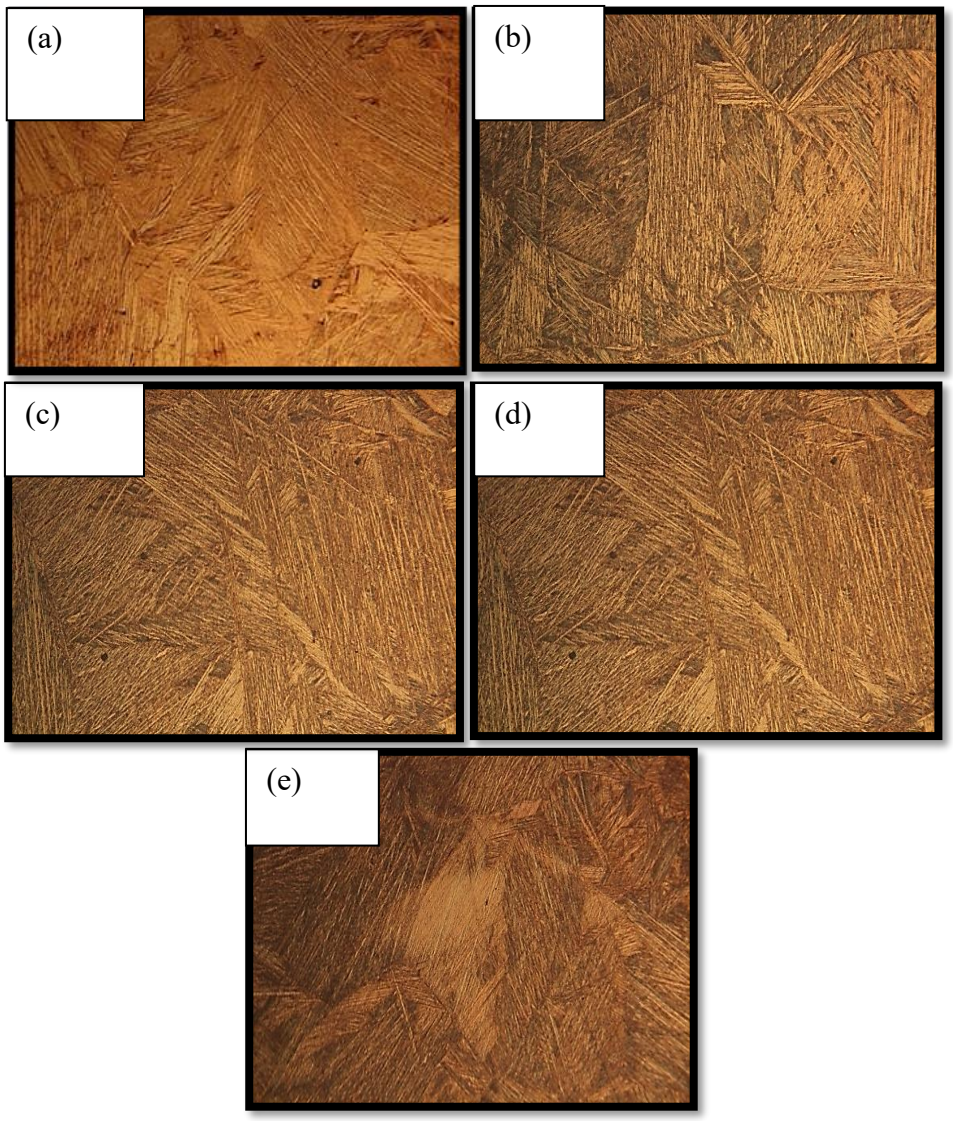

Figure 2 Optical micrographs of Cu–Al–Mn shape memory alloys with increasing Mn content: (a) CuAlMn1 (1 wt.% Mn), (b) CuAlMn2 (3 wt.% Mn), (c) CuAlMn3 (5 wt.% Mn), (d) CuAlMn4 (7 wt.% Mn) and (e) CuAlMn5 (9 wt.% Mn).

3.4. DSC analysis

A comparison of the DSC curves in Figure 3(a–e) shows a clear and progressive reduction in transformation temperatures as Mn content increases from CuAlMn1 to CuAlMn5. In Figure 3(a), CuAlMn1 displays the highest martensitic transformation temperatures, with Ms = 158.56 °C, Mf = 170.82 °C, As = 180.17 °C, and Af = 209.51 °C, indicating a strong and well-defined transformation with high enthalpy. Figure 3(b) reveals that CuAlMn2 transforms at slightly lower temperatures (Ms = 136.92 °C, Mf = 170.76 °C, As = 156.31 °C, Af = 214.76 °C), reflecting the early influence of Mn in stabilizing the β-phase. This trend becomes more pronounced in Figure 3(c), where CuAlMn3 shows

further reduced values (Ms = 132.87 °C, Mf = 158.98 °C, As = 138.60 °C, Af = 164.67 °C) and broader peaks, indicating a lower transformation driving force. A dramatic shift is observed in Figure 3(d) for CuAlMn4, where the transformation occurs near ambient conditions (Ms = 71.49 °C, Mf = 90.99 °C, As = 80.98 °C, Af = 105.82 °C), accompanied by noticeably weakened peak intensities. Finally, Figure 3(e) shows CuAlMn5 exhibiting the lowest values (Ms = 44.09 °C, Mf = 72.64 °C, As = 55.31 °C, Af = 75.33 °C) with shallow and broadened peaks, confirming significant β-phase stabilization and partial martensitic transformation [41-45]. Collectively, Figure 3(a–e) demonstrates that increasing Mn content systematically lowers transformation temperatures and reduces transformation enthalpy, underscoring Mn's dominant role in controlling phase stability in Cu–Al–Mn SMAs [42,43].

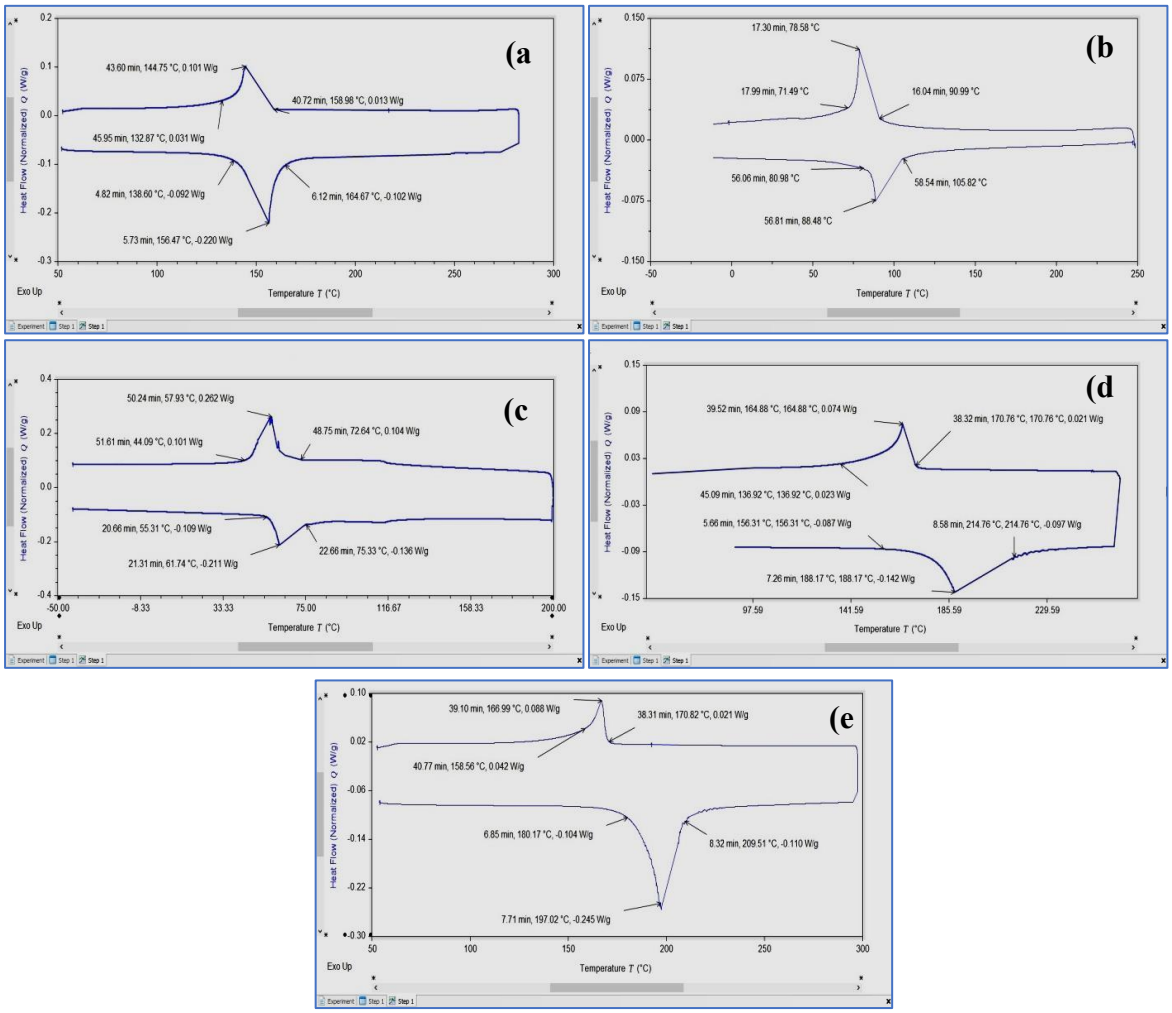

Figure 3 Differential scanning calorimetry (DSC) thermograms of Cu–Al–Mn shape memory alloys with varying Mn content: (a) CuAlMn1 (1 wt.% Mn), (b) CuAlMn2 (3 wt.% Mn), (c) CuAlMn3 (5 wt.% Mn), (d) CuAlMn4 (7 wt.% Mn), and (e) CuAlMn5 (9 wt.% Mn).

3.5. X-Ray diffraction

Figure 4 shows the X-ray diffraction (XRD) patterns of the Cu–Al–Mn alloys (a) CuAlMn1, (b) CuAlMn2, (c) CuAlMn3, (d) CuAlMn4, and (e) CuAlMn5. All samples display a similar arrangement of high-intensity reflections associated with the Cu–Al–Mn matrix phase, accompanied by several lower-intensity peaks attributed to the $AlCu_3$ intermetallic compound, marked by circular symbols in the figure. The central cluster of peaks, observed between approximately 38° and 45° in all samples, corresponds to reflections from the parent β (ordered B2 or DO3) or the transformed β1/γ1 martensitic phases typical of Cu–Al–Mn shape memory alloys. Minor reflections marked with triangles and squares represent peaks recorded at different calibration or processing temperatures (375 °C and 65 °C), confirming thermal sensitivity of the martensitic lattice. As the Mn content increases from CuAlMn1 to CuAlMn5 [44, 45], the overall peak profiles remain consistent, demonstrating that the same fundamental crystallographic framework is preserved across all compositions [46-48].

In samples (a) CuAlMn1 and (b) CuAlMn2, the diffraction peaks appear sharp and well resolved, indicating a highly ordered structure with minimal lattice distortion. These two alloys contain the lowest Mn concentrations and therefore exhibit the least deviation from the ideal β-phase lattice. The presence of clear, intense matrix peaks confirms the predominance of the β/β1 phase with only minor contributions from secondary phases. As Mn increases to (c) CuAlMn3, the peak intensities and shapes begin to change subtly, reflecting the onset of lattice contraction and increased structural distortion due to substitution of Mn atoms into the Cu sublattice. This evolution becomes more pronounced in (d) CuAlMn4 and (e) CuAlMn5, where peaks shift slightly toward higher 2θ values, indicating a decrease in interplanar spacing. These shifts are consistent with Mn's smaller atomic radius and strong electronic effects within the Cu–Al–Mn lattice, which progressively modify the unit-cell dimensions and stabilize the high-temperature β-phase [49].

Structurally, the dominant phase in all five samples corresponds to the ordered β-phase at high temperature, which transforms into martensite upon cooling. The β-phase is commonly described by a cubic crystal system and indexed using the Fm-3m space group (Heusler-type ordering). Upon cooling, this phase transforms to long-period stacking-order martensite (18R or 6R), which is often expressed in a pseudo-hexagonal representation. In this hexagonal cell, the lattice parameters satisfy $a \approx b$ and $\gamma \approx 120°$, while α and β deviate only slightly from 90°, reflecting the layered close-packed nature of the martensitic structure. Precise values of a, b, c, α, β, and γ cannot be extracted visually from the figure and require Rietveld or Le Bail refinement of the raw XRD data, but the patterns of CuAlMn1–CuAlMn5 clearly display the characteristic splitting and asymmetry associated with these martensitic polytypes [50].

The $AlCu_3$ phase detected in all samples is identified through its distinct secondary peaks and is known to crystallize in a cubic structure, typically assigned the Pm-3m space group in most JCPDS/ICDD entries. Although the exact PDF (JCPDS) card number is not visible in the figure, the pattern corresponds to well-established $AlCu_3$ reference files commonly used in Cu–Al alloy analysis. The relative increase in $AlCu_3$ peak intensity from CuAlMn1 to CuAlMn5 suggests that the amount or visibility of this secondary phase becomes more pronounced with increasing Mn content, likely due to compositional segregation or thermal effects during sintering and cooling [51,52].

Overall, the XRD patterns of Figure 4 reveal that increasing Mn content from samples (a) to (e) systematically influences peak position, intensity, and lattice distortion. These crystallographic

changes correlate directly with the microstructural refinement and the lowering of martensitic transformation temperatures observed in DSC and microscopic analyses, confirming that Mn plays a central role in modifying the structural stability and phase constitution of Cu–Al–Mn shape memory alloys [53,54].

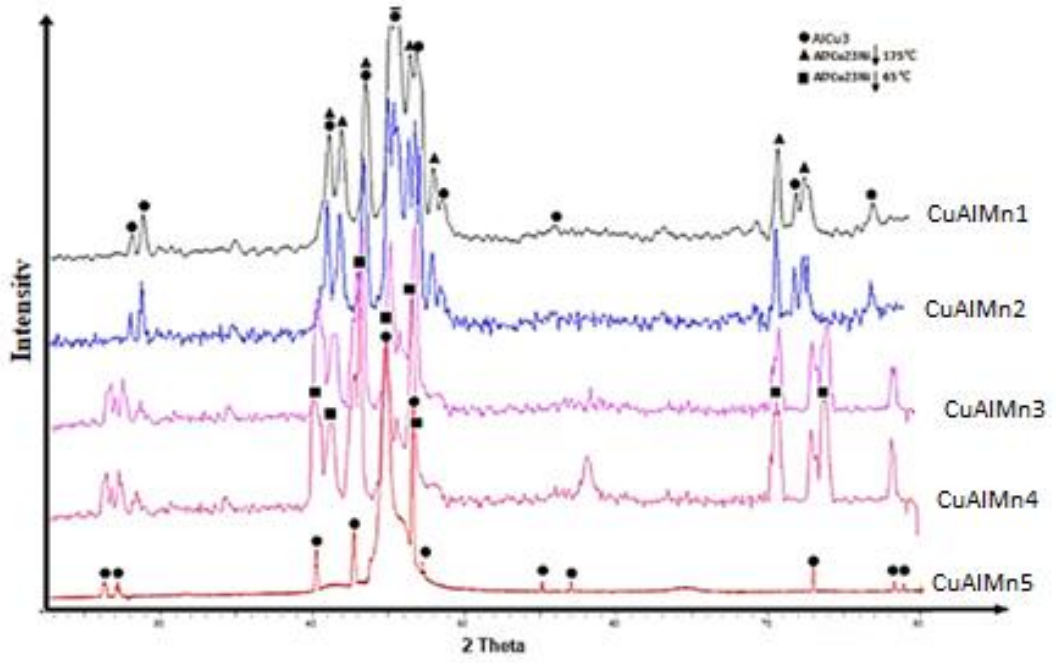

Figure 4 X-ray diffraction (XRD) patterns of Cu–Al–Mn alloys with increasing Mn content: (a) CuAlMn1, (b) CuAlMn2, (c) CuAlMn3, (d) CuAlMn4, and (e) CuAlMn5.

3.6. Hardness test

Figure 5 illustrates the effect of alloy composition on the Vickers microhardness of the Cu–Al–Mn alloys, showing a clear and consistent increase in hardness from CuAlMn1 to CuAlMn5. The measured hardness values rise from 250 HV for CuAlMn1 to 260 HV for CuAlMn2, followed by a more pronounced increase to 290 HV in CuAlMn3. This trend continues with CuAlMn4 reaching 325 HV, and the highest value, 340 HV, obtained for CuAlMn5. The progressive increase in hardness with Mn content is attributed to enhanced solid-solution strengthening, increased ordering within the β-phase, and refinement of martensitic variants as Mn stabilizes the parent phase [55, 56]. The formation of finer, more densely packed martensitic plates in higher-Mn alloys improves resistance to plastic deformation. These results are consistent with the known strengthening effects of Mn and Al in Cu–Al–Mn SMAs and confirm that compositional tuning provides a reliable pathway to increase the mechanical performance of these alloys [57,58].

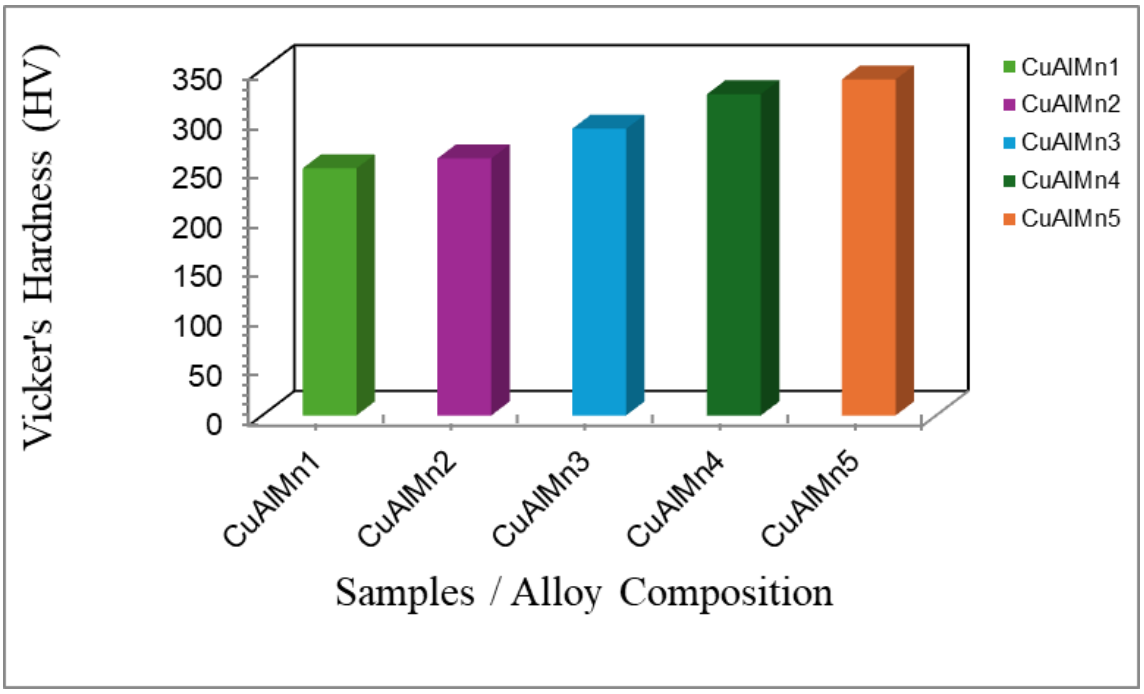

Figure 5 Variation of Vickers microhardness (HV) of the Cu–Al–Mn alloys as a function of aluminum content.

3.7. Ion release analysis

The ion-release data for the Cu–Al–Mn alloys after four weeks of immersion reveal a clear decreasing trend as Mn content increases from CuAlMn1 to CuAlMn5. The highest ion release is observed in CuAlMn1 (0.00682 ppm), followed by CuAlMn2 (0.00538 ppm). These two alloys contain the lowest Mn content and therefore exhibit the highest dissolution tendency in the test medium. In CuAlMn3, the ion-release value decreases significantly to 0.00285 ppm, reflecting a substantial improvement in chemical stability [50]. This downward trend continues for CuAlMn4 and CuAlMn5, which display the lowest release levels of 0.0021 ppm and 0.00156 ppm, respectively [51, 52]. This behavior suggests that increasing Mn content enhances the corrosion resistance and chemical stability of the Cu–Al–Mn alloys. Higher Mn levels are known to promote formation of more stable passive layers and modify the β/β_1 phase chemistry in a way that reduces matrix dissolution in aqueous environments [53, 54]. Additionally, increased Mn content tends to stabilize the martensitic microstructure, decrease intergranular degradation, and reduce galvanic activity between matrix and secondary phases [55-60]. As a result, CuAlMn5 exhibits the lowest ion release, indicating superior long-term stability and improved suitability for applications where environmental interaction must be minimized (e.g., biomedical, sensing, or marine environments [61-66]) (see Figure 6).

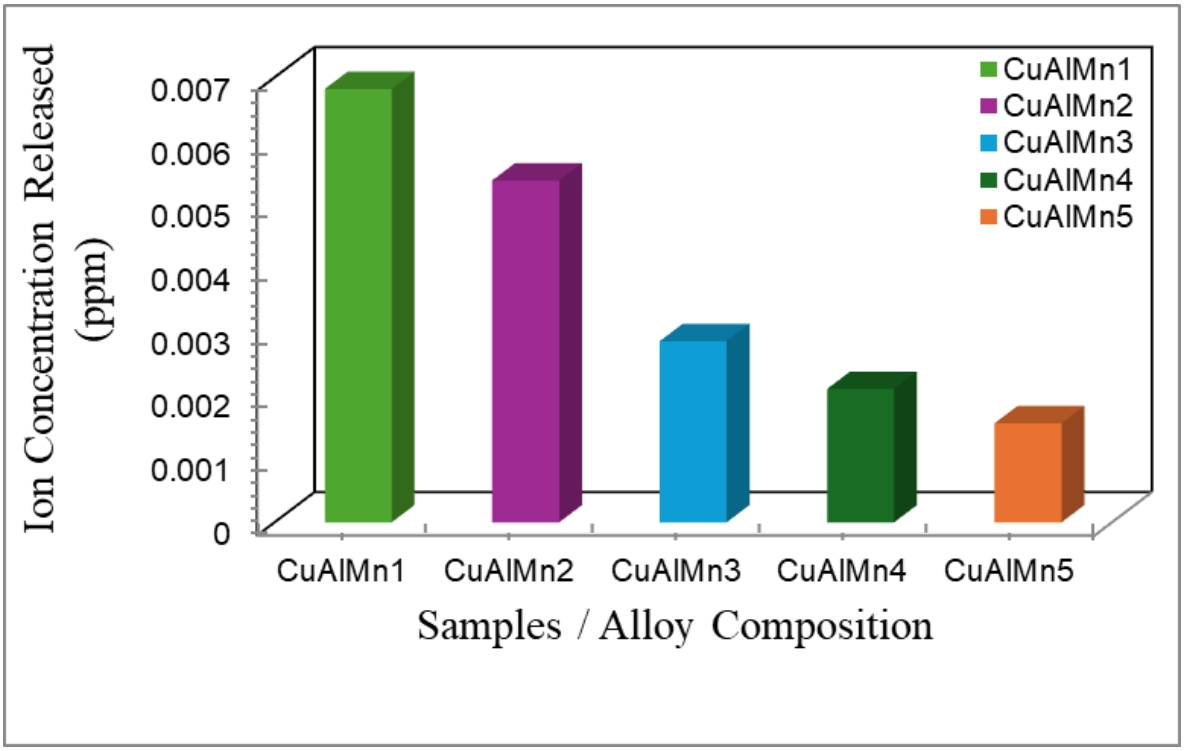

Figure 6 Ion release of Al + Mn from Cu–Al–Mn alloys after four weeks of immersion.

The SEM, optical microscopy, DSC, hardness, and ion-release results collectively demonstrate a systematic refinement of microstructure with increasing Mn content, leading to features approaching the nanoscale regime. As shown in Figures 1–3, the progressive thinning and densification of martensitic lamellae increase interface density, a key parameter in nanotechnology-driven materials design. The enhanced hardness (Figure 5) and reduced ion release (Figure 6) observed in high-Mn alloys further indicate improved surface stability and resistance to nanoscale degradation mechanisms. These findings suggest that Mn-induced microstructural refinement not only governs bulk shape memory behavior but also tailor's nanoscale surface and interface characteristics critical for functional nanotechnology applications [67-69].

Table 2 illustrates the evolution of microstructural features in Cu–Al–Mn shape memory alloys with increasing manganese content and highlights their relevance from a nanotechnology perspective. The table shows that higher Mn concentrations promote significant refinement of martensitic structures, increased interface density, and enhanced phase stability, which are key attributes for nanoscale functional performance, improved mechanical reliability, and reduced ion release in advanced smart-material applications.

Table 2 Nanotechnology-relevant features of Cu–Al–Mn SMAs as a function of Mn content.

Mn content effect	Observed microstructural feature	Nanotechnology relevance
Low Mn (1–3 wt.%)	Coarse martensitic plates	Limited nanoscale control
Medium Mn (5 wt.%)	Finer martensitic lamellae	Increased interface density
High Mn (7–9 wt.%)	Extremely fine, dense martensite with retained β-phase	Nanoscale stability, reduced ion release, enhanced surface durability

As illustrated in Figures 7 and 8, the progressive refinement of martensitic microstructures with increasing Mn content leads to enhanced nanoscale interface density, improved mechanical strength, and reduced ion release. These characteristics are essential for nanotechnology-driven applications where surface stability, miniaturization, and functional reliability are critical.

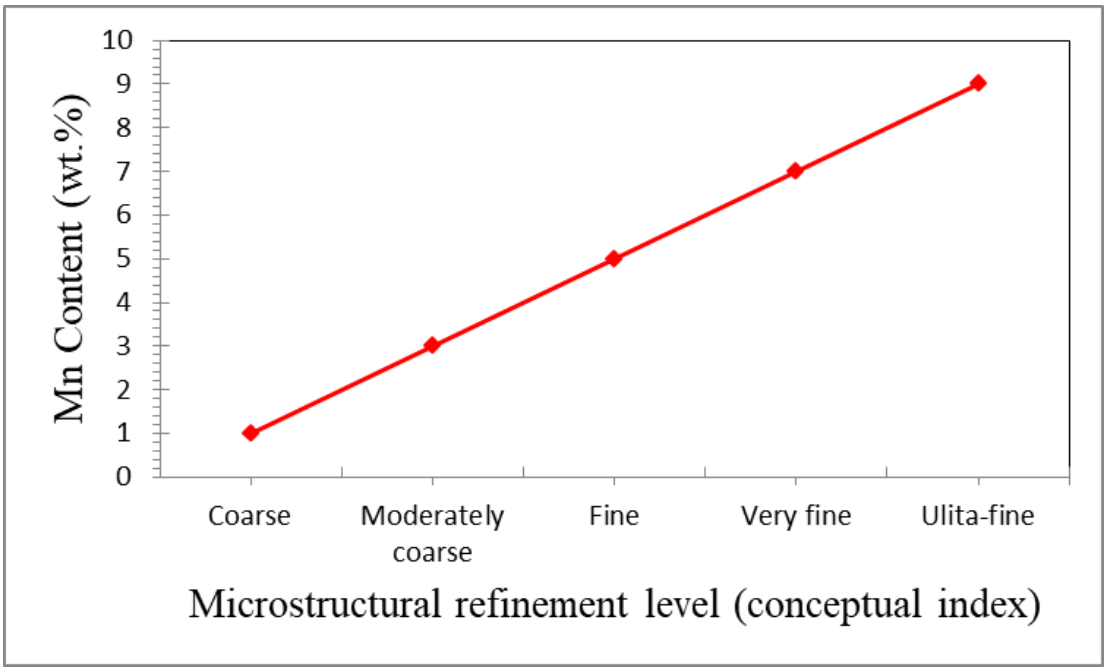

Figure 7 Effect of Mn content on microstructural refinement and nanoscale relevance.

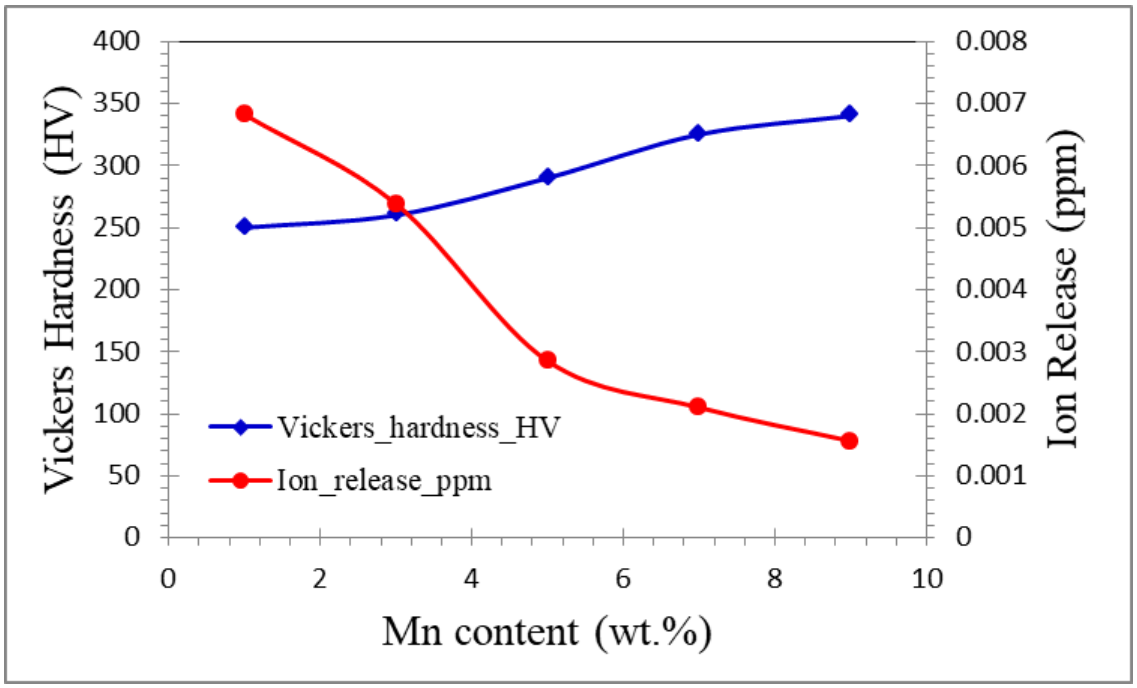

Figure 8 Hardness increase and ion-release reduction with Mn (nano-stability indicator).

4. CONCLUSIONS

This study has successfully demonstrated how varying Mn content from 1 to 9 wt.% in Cu–Al–Mn shape memory alloys significantly influences their microstructure, transformation behavior, mechanical properties, and chemical stability. Optical and SEM analyses revealed a clear refinement of martensitic morphology: CuAlMn1 exhibited coarse, widely spaced plates, while CuAlMn5 showed extremely fine, densely packed martensite with increased β-phase retention. DSC measurements confirmed the strong stabilizing effect of Mn on the high-temperature β-phase, with Ms decreasing from approximately 158.56 °C in CuAlMn1 to 44.09 °C in CuAlMn5, and Af decreasing from 209.51 °C to 75.33 °C, respectively. XRD analysis showed peak shifts toward higher 2θ values with increasing Mn, indicating lattice contraction and confirming the presence of the martensitic Cu–Al–Mn phase along with minor $AlCu_3$ intermetallic peaks across all samples. Mechanical testing further supported the influence of composition: Vickers hardness increased steadily with alloy modifications, reaching values above 330–350 HV in alloys with higher Al and Mn content. The chemical stability evaluation through ion-release testing demonstrated a substantial decrease in total Al+Mn dissolution after four weeks, dropping from 0.00682 ppm in CuAlMn1 to 0.00156 ppm in CuAlMn5, indicating superior corrosion resistance at higher Mn levels. Together, these results confirm that increasing Mn content enhances β-phase stability, refines martensitic structure, lowers transformation temperatures, increases hardness, and significantly improves chemical durability. Therefore, controlled Mn addition provides a powerful approach for tailoring the functional and structural properties of Cu–Al–Mn shape memory alloys to meet specific performance requirements in engineering and potentially biomedical applications. From a nanotechnology standpoint, this study demonstrates that manganese addition is an effective strategy for tailoring nanoscale microstructural features in Cu–Al–Mn shape memory alloys. The refinement of martensitic structures, enhancement of hardness, and significant reduction in ion release at higher Mn contents highlight the potential of these alloys for nanotechnology-enabled

applications requiring mechanical reliability and chemical stability. The results provide a foundation for the design of Cu–Al–Mn SMAs in micro- and nano-scale devices, including biomedical components, sensors, and smart actuators.

References

[1] C.J. de Araújo, A. A. C. Gomes, J. A. Silva, A. J. T. Cavalcanti, R. P. B. Reis, C. H. Gonzalez, J. mater. Proc. Tech 209 (2009) 3657. https://doi.org/10.1016/j.jmatprotec.2008.08.025
[2] T. W Duering, K.N. Melton, D. Stockel and C.M. Wayman, Eng. Asp. Shape Memo, Alloy. Butterworth – Heineman, Guildford, UK. (1990). https://doi.org/10.15209/offset.v0i10.581
[3] H. Tokunaga, Inter. J. Mater. Sci. Eng, 6 (2019) 93. https://doi.org/10.17706/ijmse.2018.6.4.93-98
[4] K. Otsuka, T. Kakeshita, Mrs Bulletin, 27 (2002) 91. https://doi.org/10.1557/mrs2002.43
[5] S. Miyazaki, K. Otsuka, C. M. Wayman, ISIJ Inter 29 (1989) 423. https://doi.org/10.2355/isijinternational.29.423
[6] F. C. Machado, Physicae, 4 (2003). https://doi.org/10.5196/physicae.4.3
[7] F. M. Braz Fernandes, K. K. Mahesh, R. J. C. Silva, C. Gurau, G. Gurau, physica status solidi (c) 7 (2010) 1348. https://doi.org/10.1002/pssc.200983371
[8] F. Amarante dos Santos, Struct. Cont. Heal. Moni, 24 (2016) e1860. https://doi.org/10.1002/stc.1860
[9] O. Sato, K. Arai, M. Shirai, Fluid Phase Equilibria, 228 (2005) 523. https://doi.org/10.1016/j.fluid.2004.08.001
[10] P. P. Lee, T. Savaskan, E. Laufer, Wear, 117 (1987) 79. https://doi.org/10.1016/0043-1648(87)90245-6
[11] I. Alshalal, H. M. I. Al-Zuhairi, A. A. Abtan, M. Rasheed, M. K. Asmail, J. Mech. Behav. Mater. 32 (2023) 1. https://doi.org/10.1515/jmbm-2022-0280
[12] M. Sellam, M. Rasheed, S. Azizi, T. Saidani, Ceram. Int. 50 (2024) 20917. https://doi.org/10.1016/j.ceramint.2024.03.094
[13] O. Alabdali, S. Shihab, M. Rasheed, T. Rashid, 3rd inter. Scient. conf. alkafeel univ. (ISCKU 2021) (2022). https://doi.org/10.1063/5.0066860
[14] M. Rasheed, O. Alabdali, S. Shihab, A. Rashid, T. Rashid, J. Phys.: Conf. Ser. 1999 (2021) 012078. https://doi.org/10.1088/1742-6596/1999/1/012078
[15] N. Assoudi et al., Opt. Quant. Electron 54 (2022) 9. https://doi.org/10.1007/s11082-022-03927-x
[16] R. Jalal, S. Shihab, M.A. Alhadi, M. Rasheed, J. Phys.: Conf. Ser. 1660 (2020) 012090. https://doi.org/10.1088/1742-6596/1660/1/012090
[17] S. Shihab, M. Rasheed, O. Alabdali, A.A. Abdulrahman, J. Phys.: Conf. Ser. 1879 (2021) 022120. https://doi.org/10.1088/1742-6596/1879/2/022120
[18] A. Keziz, M. Heraiz, M. RASHEED, A. Oueslati, Mater Chem. Phys. 325 (2024) 129757. https://doi.org/10.1016/j.matchemphys.2024.129757
[19] D. Kherifi, A. Keziz, M. Rasheed, A. Oueslati, Ceram. Int. 50 (2024) 30175. https://doi.org/10.1016/j.ceramint.2024.05.317
[20] A. Jaber, M. Ismael, T. Rashid, M. A. Sarhan, M. Rasheed, I. M. Sala, Eureka: Phys. Eng. 4 (2023) 29. https://doi.org/10.21303/2461-4262.2023.002770
[21] T. Rashid, M. M. Mokji, M. Rasheed, J. Optics (2024). https://doi.org/10.1007/s12596-024-02080-w
[22] H. K. Aity, E. Dhahri, M. Rasheed, Ceram. Int. 50 (2024) 54666. https://doi.org/10.1016/j.ceramint.2024.10.324
[23] M. Rasheed, S. Shihab, O. Alabdali, A. Rashid, T. Rashid, J. Phys.: Conf. Ser. 1999 (2021) 012077. https://doi.org/10.1088/1742-6596/1999/1/012077

[24] M. Rasheed, M. Nuhad Al-Darraji, S. Shihab, A. Rashid, T. Rashid, J. Phys.: Conf. Ser. 1963 (2021) 012058. https://doi.org/10.1088/1742-6596/1963/1/012058
[25] A. Keziz, M. Heraiz, F. Sahnoune, M. Rasheed, Ceram. Int. 49 (2023) 32989. https://doi.org/10.1016/j.ceramint.2023.07.275
[26] E. Kadri, K. Dhahri, R. Barillé, M. Rasheed. Phase Transi, 94 (2021) 65. https://doi.org/10.1080/01411594.2020.1832224
[27] D. Bouras, M. Rasheed, Opt. Quantum Electron. 54 (2022) 12. https://doi.org/10.1007/s11082-022-04161-1
[28] A. Zubaidi, L.M. Asaad, I. Alshalal, M. Rasheed, J. Mech. Behav. Mater. 32 (2023) 1. https://doi.org/10.1515/jmbm-2022-0302
[29] M. Rasheed et al., J. Phys.: Conf. Ser. 1999 (2021) 012080. https://doi.org/10.1088/1742-6596/1999/1/012080
[30] M. Rasheed, M.N. Al-Darraji, S. Shihab, A. Rashid, T. Rashid, J. Phys.: Conf. Ser. 1963 (2021) 012059. https://doi.org/10.1088/1742-6596/1963/1/012059
[31] M. Enneffatia, M. Rasheed, B. Louati, K. Guidara, S. Shihab, R. Barillé, J. Phys.: Conf. Ser. 1795 (2021) 012050. https://doi.org/10.1088/1742-6596/1795/1/012050
[32] M. Rasheed, O.Y. Mohammed, S. Shihab, A. Al-Adili, J. Phys.: Conf. Ser. 1795 (2021) 012043. https://doi.org/10.1088/1742-6596/1795/1/012043
[33] A.H. Ali, A.S. Jaber, M.T. Yaseen, M. Rasheed, O. Bazighifan, T.A. Nofal, Complexity 2022 (2022) 1. https://doi.org/10.1155/2022/9367638
[34] M. Rasheed, et al., J. Adv. Biotechnol. Exp. Ther. 6 (2023) 495. https://doi.org/10.5455/jabet.2023.d144
[35] M. Rasheed, I. Alshalal, A.A. Ashed, M.A. Sarhan, A.S. Jaber, Indones. J. Electr. Eng. Comput. Sci. 33 (2024) 653. https://doi.org/10.11591/ijeecs.v33.i1.pp653-660
[36] I.M. Mohammed, M. Rasheed, AIP Conf. Proc. 3321 (2025) 020026. https://doi.org/10.1063/5.0289719
[37] F. Boudou, A. Belakredar, A. Berkane, M. Rasheed, Not. Sci. Biol. 17 (2025) 12183. https://doi.org/10.55779/nsb17212183
[38] F. Boudou, et al., Not. Sci. Biol. 17 (2025) 12593. https://doi.org/10.55779/nsb17312593
[39] F. Boudou, A. Guendouzi, A. Belkredar. M. Rasheed, Not. Sci. Biol 16 (2024) 13837. https://doi.org/10.55779/nsb16211837
[40] R.S. Mahmood et al., J. Mech. Behav. Mater. 34 (2025) 1. https://doi.org/10.1515/jmbm-2025-0040
[41] T. Rashid, M.M. Mokji, M. Rasheed, J. Mech. Behav. Mater. 34 (2025) 77. https://doi.org/10.1515/jmbm-2025-0074
[42] M. Rasheed, M. N. Mohammedali, F. A. Sadiq, M. A. Sarhan, T. Saidani. J. Optics (New Delhi. Print) 54 (2024) 3490. https://doi.org/10.1007/s12596-024-01928-5
[43] A.J. Hussein, M.N. Al-Darraji, M. Rasheed, M.A. Sarhan, IOP Conf. Ser.: Earth Environ. Sci. 1262 (2023) 022007. https://doi.org/ 10.1088/1755-1315/1262/2/022007
[44] A.J. Hussein, M.N. Al-Darraji, M. Rasheed, M.A. Sarhan, IOP Conf. Ser.: Earth Environ. Sci. 1262 (2023) 022005. https://doi.org/10.1088/1755-1315/1262/2/022005
[45] T. Saidani, M. Rasheed, I. Alshalal, A.A. Rashed, M.A. Sarhan, R. Barillé, Res. Eng. Struct. Mater. 10 (2024) 743. http://dx.doi.org/10.17515/resm2023.21ma0922rs
[46] M. A. Sarhan, S. Shihab, B. E. Kashem, M. Rasheed, J. Phy.: Conf. Ser. 1879 (2021) 022122. https://doi.org/10.1088/1742-6596/1879/2/022122.
[47] M. Rasheed, O. Alabdali, S. Shihab, J. Phy.: Conf. Ser. 1879 (2021) 032120. https://doi.org/10.1088/1742-6596/1879/3/032120.
[48] M. Rasheed, R. Barillé, J. Non-Cryst. Solids 476 (2017) 1.

[49] M. Rasheed, R. Barillé, Opt. Quantum Electron. 49 (2017). https://doi.org/10.1007/s11082-017-1030-7.
[50] F. Dkhilalli, S. M. Borchani, M. Rasheed, R. Barille, K. Guidara, M. Megdiche, J. Mater. Sci. Mater. Electron, 29 (2018) 6297. https://doi.org/10.1007/s10854-018-8609-z.
[51] A. Boumezoued, K. Guergouri, R. Barillé, R. Djamil, M. Zaabat, M. Rasheed, J. Alloys Compd. 791 (2019) 550. https://doi.org/10.1016/j.jallcom.2019.03.251.
[52] N. Ben Azaza et al., Opt. Mater. 96 (2019) 109328. https://doi.org/10.1016/j.optmat.2019.109328.
[53] M. M. Abbas, M. Rasheed, J. Phys. Conf. Ser. 1795 (2021) 012059. https://doi.org/10.1088/1742-6596/1795/1/012059.
[54] M. Rasheed, SuhaShihab, O. Alabdali, H. H. Hassan, J. Phys. Conf. Ser. 1879 (2021) 032113. https://doi.org/10.1088/1742-6596/1879/3/032113
[55] A. S. Abbas et al., Corros. Sci. Tech. 22 (2023) 21. https://doi.org/10.14773/cst.2023.22.1.21
[56] N. S. Abtan et al., Int. J. Corros. Scale Inhib. 13 (2024). https://doi.org/10.17675/2305-6894-2024-13-1-22
[57] A. M. Resen et al., Prog. Color Color. Coat. 17 (2024) 185. https://doi.org/10.30509/pccc.2023.167189.1245
[58] A. A. Abdulhasan et al., Corros. Sci. Tech 23 (2024) 449. https://doi.org/10.14773/cst.2024.23.5.449
[59] H. K. Mohammed, A. S. Abbas, A. M. Mustafa, AIP Conf. Proc. 3002 (2024) 080030. https://doi.org/10.1063/5.0206370
[60] N. Muneam, F. F. Sayyid, M. H. H. Al-Kaabi, A. A. Alamiery, Int. J. Corros. Scale Inhib, 13 (2024). https://doi.org/10.17675/2305-6894-2024-13-1-14
[61] I. A. Annon, K. K. Jlood, N. Betti, T.S. Gaaz, M.M. Hanoon, F.F. Sayyid, A. A. Alamiery, Int. J. Corros. Scale Inhib. 13 (2024). https://doi.org/10.17675/2305-6894-2024-13-2-5
[62] A. A. Zainulabdeen et al., Int. J. Corros. Scale Inhib 13 (2024) 935. https://doi.org/10.17675/2305-6894-2024-13-2-16
[63] Z. K. Baqer, M. H. Hafiz, F. F. Sayyid, Salud Cienc. Tecnol. - Ser. Conf. 3 (2024) 832. https://doi.org/10.56294/sctconf2024832
[64] R. A. Ammar, Exp. Theo. NANOTECHNOLOGY 2 (2018) 1. https://doi.org/10.56053/2.1.1
[65] M. Mourad Mabrook, Exp. Theo. NANOTECHNOLOGY 2 (2018) 103. https://doi.org/10.56053/2.2.103
[66] F. M. Shamsudin, S. Radiman, Y. Abdullah, N. A. Hamid, Exp. Theo. NANOTECHNOLOGY 3 (2019) 27. https://doi.org/10.56053/3.1.27.
[67] D. MEKAM, D. MESRI, H. Rozale, Exp. Theo. NANOTECHNOLOGY 3 (2019) 281. https://doi.org/10.56053/3.3.281
[68] K. -O. Ong, J. Cheong, F. Heong, Exp. Theo. NANOTECHNOLOGY 4 (2020) 1. https://doi.org/10.56053/4.1.1
[69] F. M. Shamsudin, S. Radiman, Y. Abdullah, N. A. Hamid, Exp. Theo. NANOTECHNOLOGY 3 (2019) 27. https://doi.org/10.56053/3.1.27